



# Multisphere Method for Flexible Conducting Space Objects: Modeling and Experiments

Jordan Maxwell,\* Kieran Wilson,\* Joseph Hughes,\* and Hanspeter Schaub†  
 University of Colorado Boulder, Boulder, Colorado 80309

<https://doi.org/10.2514/1.A34560>

In the last two decades, concepts have been developed to harness electrostatic forces and torques to enable novel missions, including coulomb formation flying, inflating membrane structures, and detumbling and reorbiting debris touchlessly. The need for faster-than-real-time modeling of the electrostatic forces and torques in these missions has led to the development of the multisphere method (MSM) in which the electrostatic field generated by a charged body is approximated through the use of a series of optimally placed and sized conducting spheres. Although the prior work assumed the charged body was rigid, this paper extends the use of the MSM to flexible shapes. An example of the effectiveness of the MSM approach is explored by matching analytical models of the electric field and capacitance about a line of charge, and then deforming it into a ring while still matching analytic models. However, the core underlying assumption of the shape surface being a conductor remains. The limits of this model are tested via experimental comparison of a thin strip of aluminized Mylar in a constant electric field with the flexible MSM model. Although the new flexible MSM is good at modeling time-varying shapes of pure conductors, the charged thin Mylar sheet dynamics are strongly influenced by dielectric polarization and charge self-emission due to the sharp edges.

## Nomenclature

$a$	=	radius of wire, m
$d$	=	experimental plate separation distance, m
$E$	=	electric field, V/m
$E_j$	=	electric field due to sphere $j$ , V/m
$F_c$	=	coulomb force, N
$F_g$	=	gravitational force N
$F_s$	=	spring force, N
$k$	=	rotational spring stiffness, N/m
$k_c$	=	Coulomb's constant; $8.99 \times 10^9 \text{ (N} \cdot \text{m}^2)/\text{C}^2$
$l$	=	length of wire, m
$m_i$	=	mass of link $i$ , kg
$n_l$	=	number of links in discretized model
$n_s$	=	number of spheres per link in discretized model
$Q_i, Q_j$	=	charges on sphere $i$ and $j$ , C
$R_i$	=	radius of sphere $i$ , m
$r_{i,j}$	=	distance between spheres $i$ and $j$ , m
$[S]$	=	elastance matrix
$V_i$	=	voltage on sphere $i$ , V
$\Delta\theta_i$	=	relative angle between link $i$ and link $i - 1$ , m
$\theta_e$	=	unforced angle of link, rad
$\theta_i$	=	inertial angle of link $i$ , rad
$\rho$	=	radius of wire ring, m
$\tau_{e,i}$	=	electrostatic torque on hinge $i$ , N · m
$\tau_{g,i}$	=	gravitational torque on hinge $i$ , N · m
$\tau_i$	=	torque on hinge $i$ , N · m
$\tau_{s,i}$	=	spring torque on hinge $i$ , N · m

## I. Introduction

IN THE resource-constrained environment of space, the concept of low-mass and fuel-less electrostatic actuation has been considered an attractive proposition throughout the space age. Initial studies,

Received 10 June 2019; revision received 14 September 2019; accepted for publication 25 September 2019; published online 31 October 2019. Copyright © 2019 by the American Institute of Aeronautics and Astronautics, Inc. All rights reserved. All requests for copying and permission to reprint should be submitted to CCC at [www.copyright.com](http://www.copyright.com); employ the eISSN 1533-6794 to initiate your request. See also AIAA Rights and Permissions [www.aiaa.org/randp](http://www.aiaa.org/randp).

\*Graduate Research Assistant, Ann and HJ Smead Aerospace Engineering Sciences Department.

†Glenn L. Murphy Endowed Chair, Aerospace Engineering Sciences, Fellow AIAA.

originating with Ref. [1] in 1966, investigated electrostatic inflation of reflective membrane structures as a mass effective alternative to traditional deployable antennas. Later investigation of electrostatic membrane inflation has shown these forces to be sufficient to maintain inflation under orbital perturbations, with the assistance of mechanical constraints to achieve a desired shape [2,3]. The use of mechanical constraints to shape the membrane eliminates the need to model the dynamics of the system because experimental results demonstrate that the membrane will inflate satisfactorily given sufficient electrostatic pressure.

Electrostatic actuation has also been studied to control the relative motion of two or more satellite directly using continuous charge emission [4,5]. Although early papers focused on modeling the spacecraft as point charges [6–8], later work [9–17] expanded the electrostatic modeling to account for three-dimensional spacecraft shapes using the new multisphere method (MSM) approximation method to determine force and torque vectors [18–20]. The MSM is an effective means of approximating electrostatic force and torque interactions due to its low computational requirements and high accuracy [18]. Earlier work assumed the spacecraft was a rigid body with a conducting outer surface. This is a good approximation for many geosynchronous-Earth-orbit (GEO) spacecraft that have specifications to avoid differential charging across their surface. Reference [21] studied how to include hybrid conducting and dielectric outer surface materials into the MSM modeling technique. Recently, the homogeneous surface sphere constraint was relaxed, yielding a heterogeneous surface MSM (SMSM) modeling technique [22]. However, none of the prior work has accounted for time-varying space object geometries. These shape changes could be due to articular solar panels or deployable structures, or simply due to some flexing occurring across the structure. A primary goal of this paper is to expand the MSM theory to account for time-varying geometries of a charged space object and to enable rapid approximation of the resulting electrostatic forces and torques between two neighboring objects. This is of particular use to spacecraft doing orbital servicing or repair in the GEO regime where objects can naturally charge up to 1–20 kV, depending on the space weather conditions [23,24].

Beyond articulated large-scale spacecraft, a particular category of charged space objects includes high area-to-mass ratio (HAMR) debris objects found in high-altitude orbits: especially in GEO. These objects are assumed to be torn-off Mylar sheets that exhibit dynamics that are extremely difficult to model, given their usually unknown geometry and extreme flexibility. The orbits of these objects are more influenced by electrostatic perturbations than other resident space objects (RSOs), and they are strongly subject to variations in solar radiation pressure resulting from attitude variation [25]. Although the



Fig. 1 ECLIPS space environment simulation testbed.

rigid flat plate considered by Refs. [26,27] experiences extremely weak electrostatic forces and torques, the resulting accelerations can perturb the RSO's attitude to a state more strongly influenced by solar radiation pressure, which is a much more significant perturbation, leading to large changes in both position and orientation [26,28]. This paper investigates how the MSM modeling technique can be adapted to account for time varying shapes. The discretization of the surface and placement of MSM spheres to best capture local charging behavior are primary challenges.

One category of HAMR debris objects consists of aluminum-coated Mylar or Kapton sheets. As the material flexes and changes its shape, the resulting solar radiation pressure will change accordingly. In Ref. [29], the perturbed orbit of flexible Mylar was investigated. However, the sources of such flexing, which can include surface charge accumulation, were not considered in this prior work. In GEO, the relatively hot plasma environment creates conditions that can charge conducting objects to potentials as large as  $-30$  kV [27]. A crumpled sheet could become stretched out by electrostatic inflation under such conditions, dramatically changing its surface area, whereas Lorentz forces could decrease the surface area by crumpling a flat sheet. Such dramatic changes in area will significantly perturb the object's orbit by altering the effect of solar radiation pressure (SRP) and, in low Earth orbits, the atmospheric drag. By developing a novel MSM method that can handle time-varying shapes, this paper also investigates how suitable this method is for charge dynamics modeling of an aluminum-coated Mylar sheet. The challenge is that, although a flexible MSM model can account for a time-varying shape, the Mylar sheet is a dielectric with a very thin conducting surface. This means that, as the membrane is torn off, complex conducting and dielectric charging effects can occur. Furthermore, the micrometers-thin nature of the membrane raises concerns regarding charge self-emission. To study such charged membrane motion, both a numerical flexible MSM model is created and charged experiments are performed in the electrostatic charging laboratory for interactions of plasma and spacecraft (ECLIPS) facility shown in Fig. 1. This vacuum chamber is able to charge objects to multiple kilovolts using either an external power supply or an electron beam, and the resulting charged dynamical response can be visually captured through the large view ports.

The paper outlined is as follows: After summarizing the prior MSM modeling technique, the methodology is expanded to account for time-varying geometries. The accuracy and challenges are discussed by comparing the numerical response to analytical solutions of prototype examples. Next, the flexible MSM model is applied to an aluminumized Mylar sheet, which is charged inside the ECLIPS chamber. Here, the suitability of using this modeling technique to predict the thin membrane motion is investigated.

## II. Review of the General MSM Technique

The MSM is an accurate, computationally efficient method of approximating the electrostatic interactions between conductors. The general shape is discretized into a series of body-fixed spheres for which the radii are chosen such that the resulting electrostatic behavior matches that of the continuous shape. Two main categories of MSM exist: the volume MSM (VMSM), and the SMSM [19]. The VMSM requires that both sphere radii and placement are optimized to match forces and torques [18], capacitance [30], or electric fields [20]. The SMSM, on the other hand, places spheres equidistantly on the surface of the modeled object; and it optimizes only the sphere radii to match any of the physical quantities listed previously. For the investigation to follow, an equidistant SMSM model using capacitance matching is employed. A comparison of the resulting electric fields validates this model calibration method.

A significant challenge of applying the MSM on orbit is the development of MSM models for poorly understood objects such as debris. Several solutions to this problem have been proposed. One analyzes orbital perturbations due to coulomb interactions between a servicer craft for which the voltage is known and a debris object to determine the charge distribution on the debris and develop an MSM model [31]. Another uses a dual-Langmuir probe system on board a servicer craft to determine the proper MSM model for a rotating craft or object [32]. Additional recent work in this area has introduced two new methods for determining the relative potential between two craft: one uses secondary electron emission to estimate the target craft potential [33], whereas the other uses x-ray spectroscopy to generate a map of surface potential distributions on the target [34].

Figure 2 depicts the MSM concept. The voltage on each of the spheres shown is related to the charge on that sphere by

$$V_i = k_c \frac{Q_i}{R_i} + k_c \sum_{j=1, j \neq i}^n \frac{Q_j}{r_{i,j}} \quad (1)$$

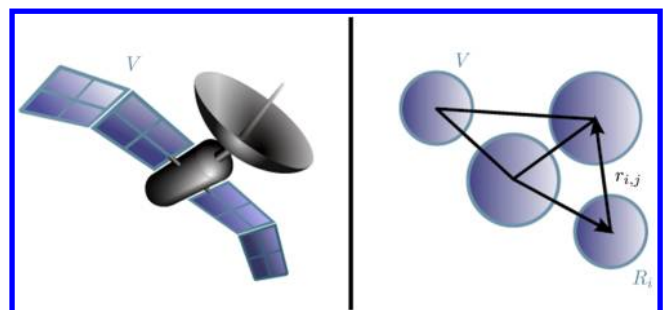


Fig. 2 Replacement of complex geometries with MSM spherical shells.

where  $k_c = 8.99 \times 10^9 \text{ (N} \cdot \text{m}^2)/\text{C}^2$  is Coulomb's constant,  $R_j$  is the radius of the  $j$ th sphere, and  $r_{i,j}$  is the distance between the  $i$ th and  $j$ th spheres. These relations are rewritten into the following single matrix equation:

$$\begin{pmatrix} V_1 \\ V_2 \\ \vdots \\ V_n \end{pmatrix} = k_c \begin{bmatrix} \frac{1}{R_1} & \frac{1}{r_{1,2}} & \cdots & \frac{1}{r_{1,n}} \\ \frac{1}{r_{2,1}} & \frac{1}{R_2} & \cdots & \frac{1}{r_{2,n}} \\ \vdots & \vdots & \ddots & \vdots \\ \frac{1}{r_{n,1}} & \frac{1}{r_{n,2}} & \cdots & \frac{1}{R_n} \end{bmatrix} \begin{pmatrix} Q_1 \\ Q_2 \\ \vdots \\ Q_n \end{pmatrix}, \quad \mathbf{V} = [\mathbf{S}]\mathbf{Q} \quad (2)$$

The matrix  $[\mathbf{S}]$  is called the elastance matrix [35]. The charge to voltage relationship of  $\mathbf{Q} = [\mathbf{C}]\mathbf{V}$  illustrates that the capacitance is the inverse of the elastance matrix:

$$\mathbf{Q} = [\mathbf{S}]^{-1}\mathbf{V} \quad (3)$$

This form is preferable in the electrostatic force and torque evaluation process because the voltage is usually known and the dynamics are dependent on charge. For a single rigid structure, the capacitance matrix is constant. If multiple rigid bodies are modeled, then diagonal blocks of the elastance matrix that, when inverted, represent the self-capacitance of each rigid body, are constant; whereas the offdiagonal blocks vary with time as the relative positions of these bodies varies [18–20]. An expansion to consider a flexible structure also requires a time-varying elastance matrix. The MSM radii  $R_j$  are held constant, but the relative distances  $r_{i,j}$  change as the object flexes. In contrast to prior work, even the self-capacitance matrix of such a flexible object will now vary with time.

The basic approach taken to evaluate a time-varying MSM model is as follows; to adjust the existing MSM electrostatic force and torque modeling technique to a body with a time-varying shape, the body is first decomposed into a finite set of surface segments. The relative degrees of freedom between these surface elements are assumed to be known, i.e., how one element rotates or hinges relative to another element. Next, either a VMSSM or SMSM model is created for each shape element, placing the charge spheres at fixed locations on this element. As the shape changes and the relative position of the rigid elements vary with time, the locations of the spheres to those on other elements must be updated at each time step. This creates a time-varying elastance matrix that is readily calculated using the MSM modeling technique. This modeling approach is justified because Poisson's electrostatic field equation allows for the superposition of the charge solution, as is demonstrated using a line of charge deformed into ring. This superposition allows the MSM to model the electric field between neighboring RSOs. Losses in numerical accuracy occur because the MSM model is only an approximation of the true electric field about this shape segment. However, prior work has shown that, for two bodies separated by distances on the order of the spacecraft dimensions, these approximations have errors in the electric field of 1% or less [20]. The accuracy for this flexible approach is thus determined through both the number of shape segments (i.e., the finite element meshing) and the number of spheres used to represent the electric field of an individual mesh element.

To illustrate how this flexible shape MSM is set up, consider Fig. 3. For this case, it is assumed that the radii of the MSM spheres are all similar, but this is not a necessary condition. The charge–voltage relationship is then set up with the MSM formulation to yield the following elastance matrix:

$$\begin{bmatrix} V_1 \\ V_2 \\ V_3 \end{bmatrix} = k_c \begin{bmatrix} \frac{1}{R} & \frac{1}{r_{1,2}} & \frac{1}{r_{1,3}} \\ \frac{1}{r_{2,1}} & \frac{1}{R} & \frac{1}{r_{2,3}} \\ \frac{1}{r_{3,1}} & \frac{1}{r_{3,2}} & \frac{1}{R} \end{bmatrix} \begin{bmatrix} Q_1 \\ Q_2 \\ Q_3 \end{bmatrix} \quad (4)$$

The diagonal elements of the elastance matrix remain constant as the body flexes, whereas the offdiagonal elements must be updated at

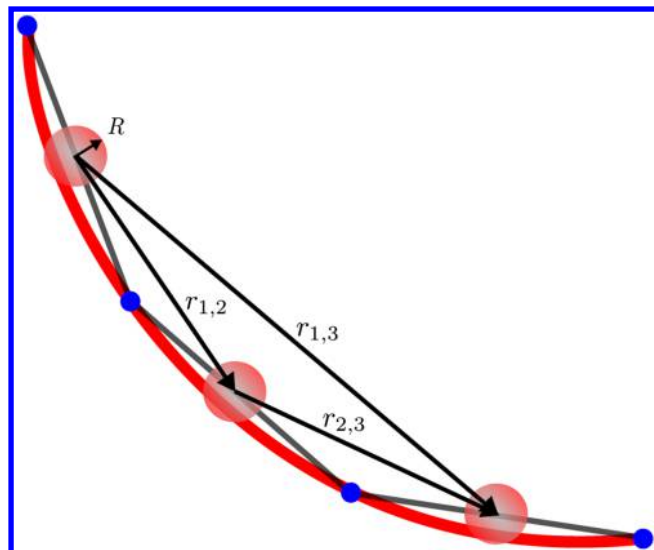


Fig. 3 MSM model of multilink pendulum.

each time step with the current relative positions of the surface elements.

### III. Comparison to Analytical Electric Field and Capacitance Solutions

This paper applies the flexible MSM concept to a one-dimensional flexible conducting wire because there are a select few analytical solutions. However, the methodology readily applies to general shapes. Figure 3 shows such a wire object modeled as a multilink pendulum with MSM spheres placed at the center of each link. Analytic solutions for the capacitance and electric field for both straight lines of uniform charge and rings of charge are known, and so the accuracy of the MSM model can be assessed for these configurations.

The capacitance of a long, thin, straight wire was given by Ref. [36] as

$$C = \frac{l}{k_c \Lambda} \left[ 1 + \frac{1}{\Lambda} (1 - \ln 2) + \frac{1}{\Lambda^2} \left( 1 + (1 - \ln 2)^2 - \frac{\pi^2}{12} \right) + \mathcal{O}\left(\frac{1}{\Lambda^3}\right) \right] \quad (5)$$

where

$$\Lambda = \ln\left(\frac{l}{a}\right) \quad (6)$$

The variable  $l$  is the length of the wire, and  $a$  is its radius. This equation is valid for large  $\Lambda$ , which requires that the wire length is much greater than the radius. This scalar capacitance value is used to optimize the sphere radius  $R$  used in the model. The comparison to the capacitance described in Eq. (3) is accomplished by summing the members of the matrix capacitance as in Eq. (7):

$$C_{\text{scalar}} = \sum_{j=1}^n \sum_{i=1}^n C_{i,j} \quad (7)$$

If the wire changes shape, Eq. (5) no longer holds. However, the optimization to generate the sphere radii for the diagonal of the elastance matrix is computationally expensive, and determining the nominal capacitance to which to optimize is nontrivial for complicated shapes such as a flexing wire. The error resulting from holding these diagonal components constant while letting the offdiagonal terms in Eq. (4) vary as the shape changes is investigated to determine if reoptimization is necessary.

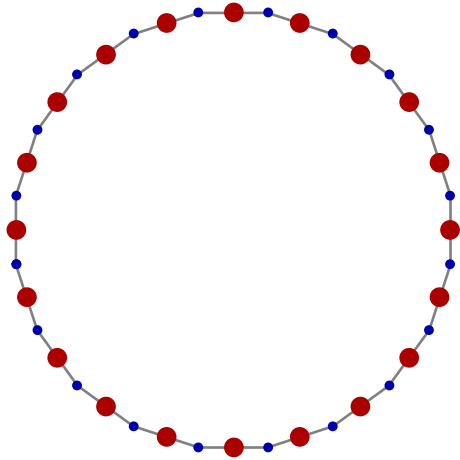


Fig. 4 Twenty-link SMSM model of an anchor ring. Blue circles indicate hinge locations, whereas red accurately represents the SMSM sphere radii optimized using Eq. (5).

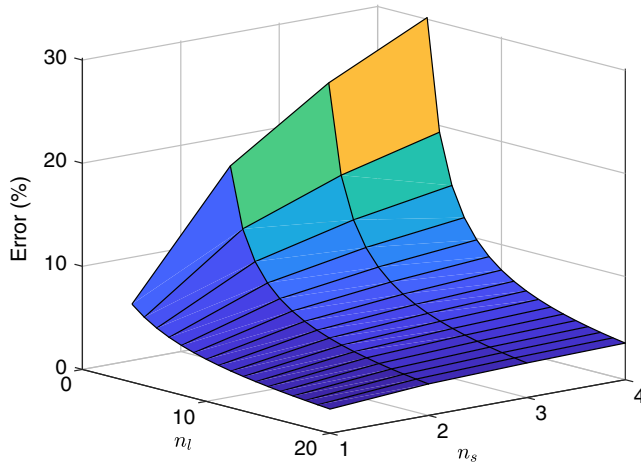


Fig. 5 Percent difference between the SMSM and analytic anchor ring capacitance for various numbers of links and MSM spheres.

In addition to the straight line, an analytical approximation exists for the capacitance of an anchor ring with uniform charge. Reference [37] showed that the capacitance of a charged ring for which the cross-sectional radius  $r$  is small as compared to the ring radius  $\rho$  is

$$C = \frac{\pi\rho}{k_c \ln(8\rho/r)} \quad (8)$$

Two configurations of a 20-link system similar to that shown in Fig. 3 are compared. First, the link is arrayed as a 3 m straight line, and the SMSM sphere radii are optimized to match the capacitance in Eq. (5). The SMSM system is then rearranged into a ring shape of radius  $\sim 0.5$  m (calculated by equating the length of the wire and circumference of the ring), as in Fig. 4, without changing the SMSM sphere locations within each link or the sphere radii to match the capacitance of the ring. The offdiagonal terms of the capacitance matrix account for this new geometry, and the sum of all matrix elements is compared to the analytical result in Eq. (8).

Figure 5 shows the error between the SMSM capacitance derived from the process described and the analytic ring capacitance in Eq. (8) for a given number of links  $n_l$  and number of spheres on each link  $n_s$ . Note that, for a 20-link system, the SMSM capacitance matches the analytic to within 3%, although high accuracy is still achieved in lower-fidelity models. Interestingly, the addition of more spheres on a given link (i.e., the cases where  $n_s > 1$ ) negatively impacts capacitance matching. A larger number of spheres per segment provides a better model of the  $n_l$ -sided polygon, and not the true circular shape. Thus, if a continuous deflection is modeled with the flexible MSM

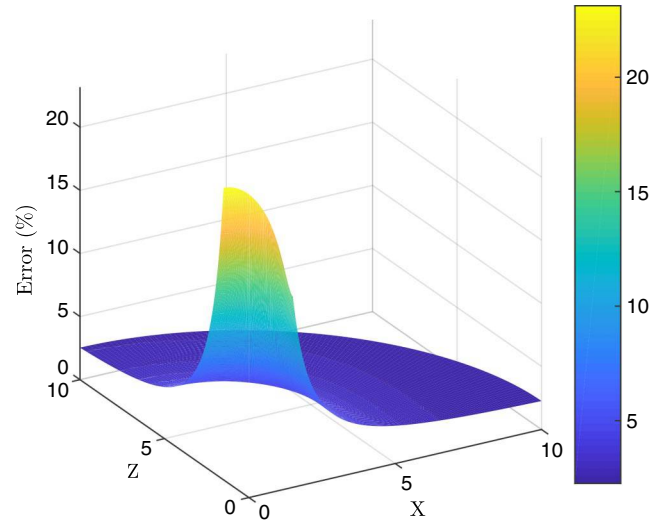


Fig. 6 Percent difference between electric field magnitudes for a 20-link SMSM model and analytic anchor ring approximation.  $X$  and  $Z$  axes are in units of the ring radius ( $\sim 0.5$  m).

approach, only a single sphere should be assigned per segment. Higher accuracy is achieved by incorporating more segments. On the other hand, if the time-varying shape is due to the articulation of a rigid component of a solar panel, then adding more spheres to the panel model can improve overall accuracy. For this reason, all future discussions for the continuous wire model deflections consider only a single MSM sphere on a given link of the model. The high accuracy discussed indicates that the capacitance can be well approximated by an SMSM model without reoptimizing at each time step.

The accurate capacitance matching indicates that, for a given voltage, the total charge on the SMSM model will match that on an anchor ring. However, the goal of the flexible MSM is to accurately model dynamics resulting from electrostatic interactions. This requires that the electric fields match as well. Reference [38] presented a method for approximating the electric field near a ring of charge. This is compared with the SMSM model's electric field, calculated via superposition of the individual field of each MSM sphere.

Figure 6 shows the percent difference between the two electric fields of the same  $\sim 0.5$  m radius ring discussed previously, which is charged to 1 kV. The distances along the  $X$  and  $Z$  axes are displayed in units of the ring radius. For this coordinate system, the  $Z$  axis is aligned with the anchor ring's axis and  $X$  lies in the plane of the picture in Fig. 4. The origin of the system is at the edge of the anchor ring (i.e., the space inside the ring is not analyzed). Because an anchor ring exhibits symmetry about its axis, so does its electric field. Therefore, the complete field can be analyzed by consideration of the single plane pictured in Fig. 6.

Note that, for distances less than approximately two ring radii, the electric field error is large due to the discrete nature of the charge distribution present in the SMSM model but not in the approximation presented in Ref. [38]. At farther points, the error converges to the same 3% exhibited by the capacitance as shown in Fig. 5. Although various proximity operations are subject to different model error constraints, an accuracy of less than 5% at a few body radii after significant deformation indicates that, for this system, there is no need to reoptimize the MSM model as deformations occur.

#### IV. Experimental Comparison to Numerical Simulation

To test the applicability of the flexible MSM technique to modeling a HAMR-like object, numerical simulations of a flexible conducting strip are compared to experiments of strips of charged aluminized Mylar deflecting in a constant electric field. A conducting one-dimensional aluminized Mylar strip at a known surface potential is held vertically in a flat electric field within a vacuum chamber. As the potential of the strip and the magnitude of the imposed electric field

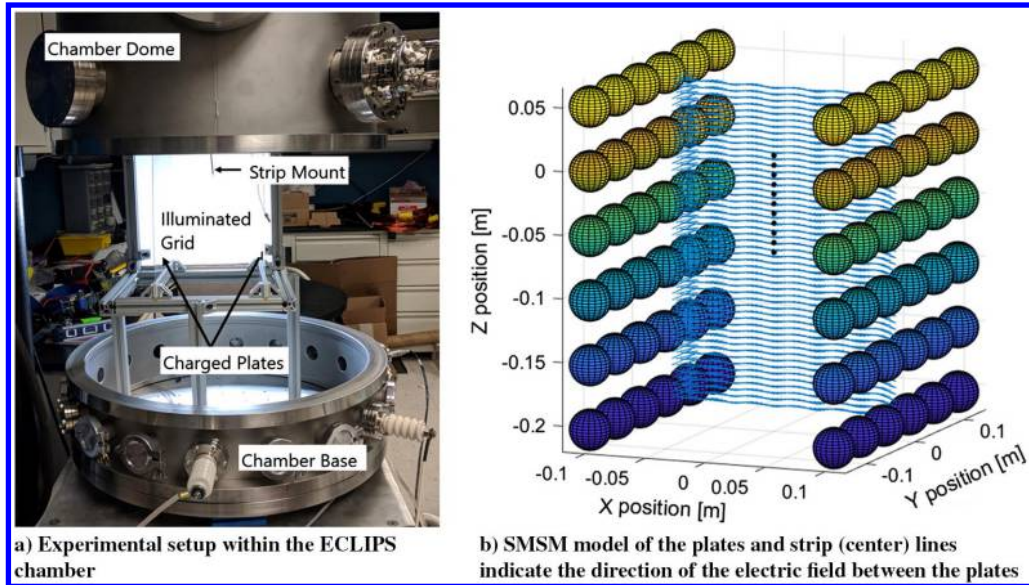


Fig. 7 Experimental setup illustration.

are varied, the strip exhibits shape and position changes. A numerical simulation employing an MSM model like that pictured in Fig. 3 yields predicted dynamics that are compared to the empirical results.

#### A. Experimental Setup

The experiment outlined previously was constructed in the ECLIPS facility photographed in Fig. 7. Prior experiments conducted at atmospheric pressure demonstrated the deflection of a Mylar strip under electrostatic forcing. However, lessons learned from those tests (including susceptibility to ionizing the air around the strip, and thereby affecting the strip dynamics) motivated the decision to conduct experiments in vacuum [39]. Experiments were conducted at pressures below  $10^{-6}$  torr to avoid electrostatic discharge events due to atmospheric ionization.

Figure 7a shows the experiment setup, consisting of a thin aluminized Mylar strip (used to approximate a one-dimensional flexible structure) held at a prescribed potential between two parallel aluminum plates. These plates acted as a parallel plate capacitor to generate an approximately flat electric field in the region of the strip. A SSM model of the plates is used to explore the uniformity of the electric field between the plates, as illustrated in Fig. 7b.

A highly flexible conductor is assumed in the numerical simulations; however, an aluminized Mylar strip is used for the actual experiments. Commercially available thin metal membranes were considered, but purely metallic films lack the flexibility required to exhibit significant elastic deformation. Because these experiments are designed to investigate the application of the flexible MSM to charged time-varying membranes, significant shape change is desired. Of the various materials considered, only aluminized Mylar exhibited this behavior. This material consists of two coatings of 100-Å-thick aluminum on either side of  $7\ \mu\text{m}$  Mylar substrate, which introduced its own complexities to the experiment. The aluminum coatings normally isolated by the Mylar were both electrically connected to the power supply. Additionally, although a pure conductor is simulated, the experimental strip consists of a mixture of dielectric and conductive components. Furthermore, the strip is not a true one-dimensional structure but, instead, has dimensions of  $7.2 \times 0.1$  cm, and so it is possible for the strip to rotate in addition to bending: a factor not accounted for in the planar numerical models. To increase the scale of the deformations seen and reduce the impact of rotational deformations, the Mylar strip was folded to introduce a kink at the center of the strip.

The strip is suspended midway between the cathode and anode of the parallel plate capacitor. This configuration allows different potentials to be applied to the cathode of the capacitor (controlling the electric field) and to the strip, creating a spacelike scenario, where

environmental currents to RSOs are not necessarily dependent on the local electromagnetic fields. The anode plate is connected to the facility ground.

Two separate power supplies are used to control the potential of the strip and the cathode. A Spellman CZE2000 high-voltage power supply (HVPS) is used to establish the potential of the strip, whereas an SL300 HVPS sets the potential of the cathode of the parallel plate capacitor. The CZE2000 is computer controlled through a LabView script interfacing with a National Instruments Universal Serial Bus (USB) data acquisition unit.

A SSM model of the plates and strip is used to verify that a flat, constant electric field is generated by the parallel plate capacitor. Figure 7b illustrates the experimental setup as modeled in the numerical simulation, with the direction of the electric field shown by the lighter blue lines between the plates: in this case, for  $\Delta V = 1000$  V. The field in the region of the strip is close to the well-known parallel plate capacitor equation for the electric field of  $E = (\Delta V/d)$ , where  $d$  is the plate separation. Note that Fig. 7b shows that the electric field between the plates is flat everywhere except near edges. The aluminized Mylar strip was therefore centered between the plates, far from any edges in all experiments. The position of the uncharged strip can be seen as the small, dark spheres in Fig. 7b.

#### B. Analysis of Experimental Results

The voltages of the cathode plate and the strip were varied independently, and a photograph was taken of the equilibrium position of the strip. Four tests are compared, ranging from 0 to 3000 V on the strip and either 0 or 1000 V on the cathode of the capacitor. The experiment charging cases are listed in Table 1. When the voltage on the strip was increased (from 0 to 1000 V, for example), the strip would typically flutter for less than 5 min before damping out to its steady-state position. To improve the ability to photograph the strip from outside the chamber, a translucent Delrin sheet was placed behind the strip and illuminated from behind. This resulted in a diffuse backillumination source for consistent photographs. Additionally, a hole pattern of known spacing was drilled into the Delrin sheet. The resulting pinpricks of light allowed a consistent

Table 1 System voltages for experiments

Run no.	Plate voltages, V	Strip voltages, V
1	0	0
2	1000	1000
3	1000	2000
4	1000	3000

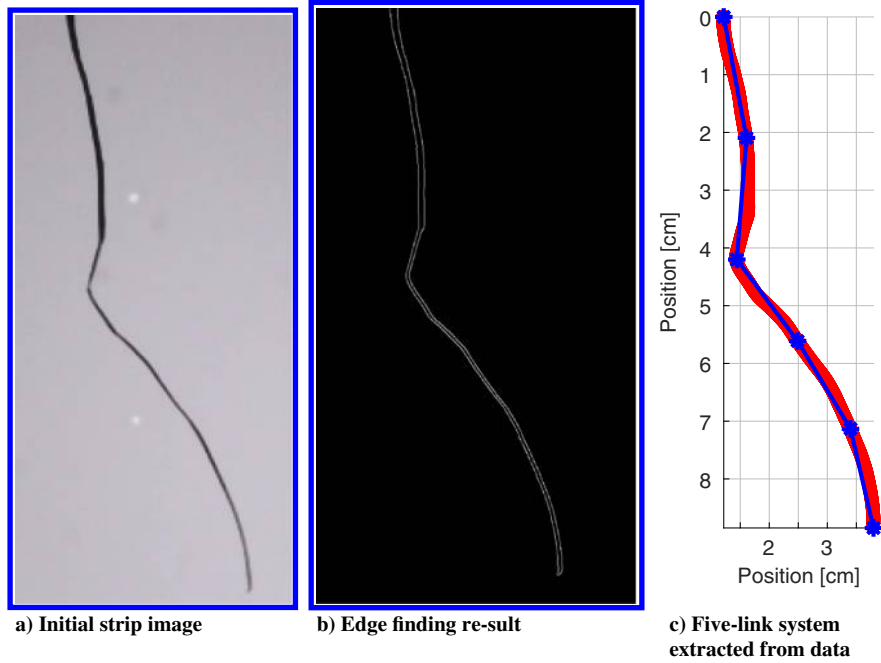


Fig. 8 Image analysis results.

conversion from image pixels to centimeters. These holes can be seen in Fig. 8 along with the unprocessed strip image.

Edge finding algorithms in the MATLAB Image Processing toolbox were used to differentiate the strip from the Delrin sheet. The orientation of the grid points in the Delrin sheet provided an arbitrary vertical axis to which the image can be aligned, eliminating the need to align the camera itself. After isolating the strip edges as seen in Fig. 8, the positions of the edges were averaged at each  $y$  value to find the centerline. The resultant centerline data were smoothed using a Gaussian-weighted moving average filter to reduce high-frequency noise before curve fitting. The data were then divided into two segments, split by the kink that had been introduced near the middle of the Mylar strip. A piecewise cubic Hermite interpolating polynomial was then fit to the smoothed data on each side of the strip.

Once the interpolating function is obtained, it is used to develop a discrete  $n$ -link system for comparison with the  $n$ -link model. The choice of  $n = 11$  represents a reasonable balance between the convergence speed for numerical simulation and model fidelity. Finally, the positions of the hinges are found via discretization of experimental data for comparison to numerical simulations.

### C. Flexible MSM Wire Numerical Simulation

The strip is modeled using a flexible MSM as described previously. As illustrated in Figs. 3 and 9, the flexible conducting wire studied is approximated as a multilink pendulum system with SMSM spheres placed at the center of each link. In Fig. 9, a single force is shown at each sphere position for clarity; but, in the model, all three forces are applied at all three locations. The sphere position is held at the link center due to the symmetry of the simple shape segments. As discussed previously, the addition of more MSM spheres on a single link led to departures from the analytic expressions presented, and so a one-sphere-per-link model was implemented. To account for the stiffness of the wire, torsional springs are simulated at the hinge points of the model. This modeling method was chosen because it has been successfully applied to similar, highly flexible objects such as tethers [40]. It was noted during experiments that the Mylar strip has small wrinkles that change the local stiffness from segment to segment. Furthermore, the intentional bend in the middle of the strip introduces a particular deformation that is well modeled with a dedicated spring stiffness. Alternative approaches such as a deflected-beam model were discarded because they are valid only for simple geometries and small deflections. The following experiments violate both of these assumptions.

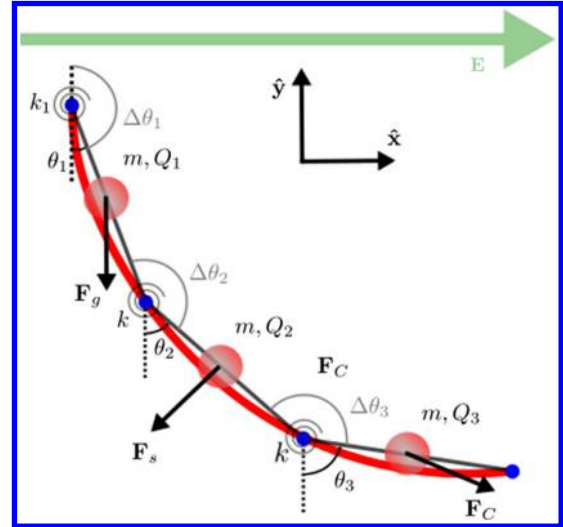


Fig. 9 SMSM model of a wire showing forces.

The transient dynamics of the strip are not of interest here. Instead, the equilibrium position of the strip under a given charging condition will be compared to the experiment. Therefore, the full differential equations of motion for the strip do not need to be solved in time. Rather, the equilibrium position of the multilink pendulum system can be determined as the set of link angles  $\theta_i$  for which the torque at each link  $\tau_i$  goes to zero. Given the experimental setup, the total torque on each hinge is given as

$$\tau_i = \tau_{s,i} + \tau_{g,i} + \tau_{e,i} \quad (9)$$

where the spring  $s$ , gravitational  $g$ , and electrostatic  $e$  torques are calculated as

$$\tau_{s,i} = k_i(\Delta\theta_i - \Delta\theta_{0,i})\hat{n} \quad (10)$$

$$\tau_{g,i} = \sum_{j=i}^n \mathbf{r}_{ij} \times m_j \mathbf{g} \quad (11)$$

$$\tau_{e,i} = \mathbf{r}_i \times q_i \mathbf{E} + \sum_{j \neq i}^n \mathbf{r}_{ij} \times q_j \mathbf{E}_j \quad (12)$$

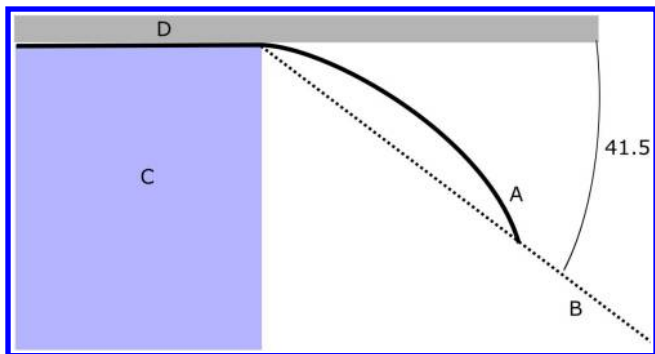


**Fig. 10** Experimental setup used to determine initial values of torsional stiffness.

where  $r_{ij}$  is the position vector from the  $i$ th hinge to the  $j$ th mass or charge. The spring torque on a given hinge in Eq. (10) is proportional to the difference in the current deflection angle  $\Delta\theta$  and its equilibrium orientation  $\Delta\theta_0$ . The torque due to gravity on a given hinge is a function of the gravitational force on all links below that hinge, as described by Eq. (11). The electrostatic torque in Eq. (12) is a sum of the torque due to the external electric field  $\mathbf{E}$  and the fields generated by the other MSM spheres  $\mathbf{E}_j$ . A schematic of the model and forces is shown in Fig. 9. The direction of the gravitational force  $\mathbf{F}_g$  does not change, whereas the coulomb and spring forces  $\mathbf{F}_C$  and  $\mathbf{F}_s$  change as the strip deforms. The direction of the coulomb force changes in time because, in addition to the static electric field in the  $\hat{x}$  direction, mutual coulomb repulsion is applied at each sphere. This is accounted for in the direction of  $\mathbf{F}_C$  in Fig. 9.

Two tunable parameters exist at each hinge: the equilibrium angle  $\Delta\theta_0$ , and the spring stiffness  $k$ . For a strip discretized into  $n$  links, this results in  $2n$  unknown parameters required to model the strip. To uniquely determine the values of these parameters therefore requires fitting the model to two separate experimental trials, providing  $2n$  points to match.

Values of  $k$  used to initialize the optimizer were found through an experimental procedure, with the setup illustrated in Fig. 10, and adapted from the American Society for Testing and Materials (ASTM) testing standard as described in Ref. [41].

As shown in Fig. 10, a strip of Mylar (point A) was cantilevered over the edge of a table (point C), and the cantilever length progressively increased until the tip of the strip touched a line inclined at 41.5 deg with respect to the tabletop. Based on the mass of the material and the length of the cantilever required to reach that angle, equations are available as a part of the ASTM testing standard [41] to determine the stiffness of the strip. For the Mylar strip here, the stiffness was found to be approximately  $1.4 \times 10^{-6}$  N · m. This value is used to initialize the multilink model discussed previously.

Initializing the multilink model to match the experiment discussed previously, the first link is taped to the mount, forcing a different stiffness at that point than others. Likewise, the kink point has had material properties altered by the plastic deformation introduced to generate more significant changes in strip shape. In addition to these points of known variation, the thin and lightweight nature of the Mylar strip resulted in significant heterogeneity in stiffness from one point on the strip to another. This could be the result of varying edge effects as a result of cutting the strip to size or wrinkles already present in the material, which can induce twisting behaviors to the strip.

After obtaining the positions of each hinge for each experiment and an initial guess for the stiffness of the strip as described previously, the numerical simulation can be tuned. Two datasets must be used to obtain a unique solution given the  $2n$  parameter space. This is done through the use of MATLAB's `fmincon` function, which is a constrained nonlinear, multivariate optimizer. The stiffness parameters are initialized using the experimentally computed stiffness of the strip, whereas the uncharged case relative angles are used to initialize  $\theta_e$ . The function then computes the anticipated position of the two fitting cases, based on the spring, gravitational, and electrostatic torques on each link. A second solver is then used to determine

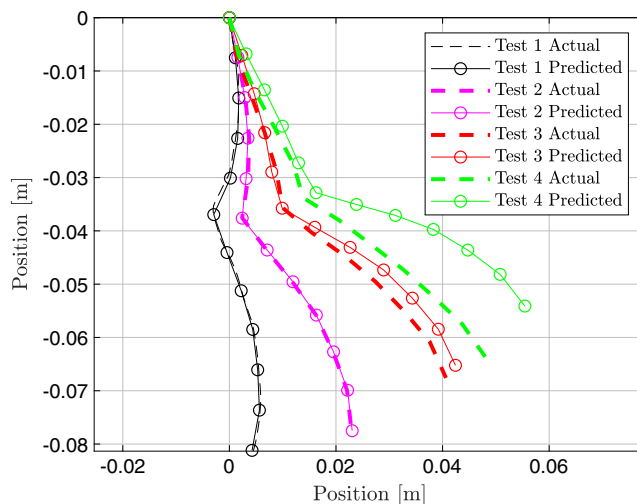


**Fig. 11** Results of tuning the model to runs 1 and 2, as well as predicting the positions of runs 3 and 4.

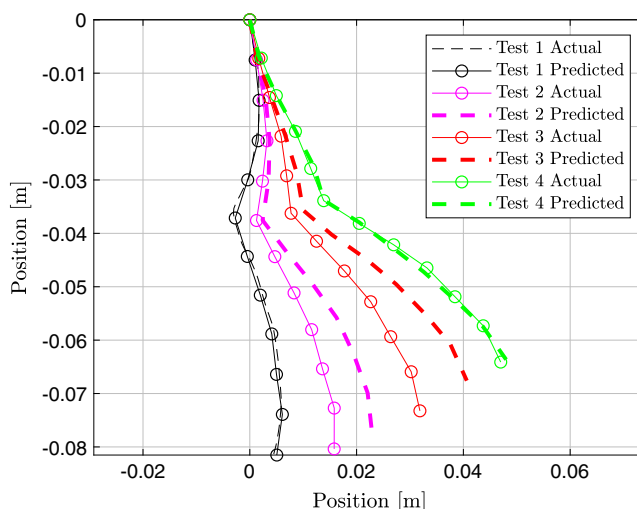
the position of each hinge, which minimizes the torque; and then the resultant hinge positions are compared to the experimental results for that set of conditions. The top-level optimizer then iterates, altering  $k$  and  $\theta_e$  until there is close agreement between the positions of the two experimental cases and their numerically simulated counterparts. Eventually, a tuned value of each of the parameters is determined for each hinge.

Using these parameters and the voltage conditions of the other two tests, the hinge locations were again calculated to determine the angles that would minimize the torque on each hinge. This then allowed tests beyond the range of the two tuning runs to be modeled, with the results shown in Fig. 11.

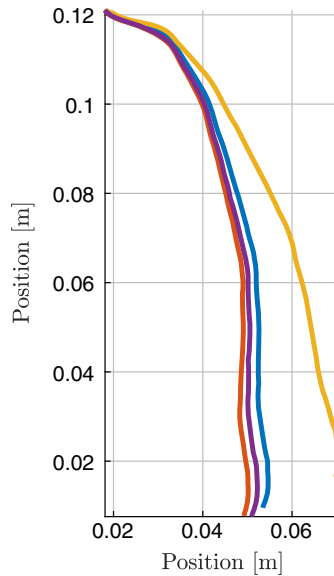
## V. Results and Discussion

Table 1 shows the voltage levels for each experiment conducted. The plate voltage is applied to the cathode of the parallel plate capacitor while the anode is set to ground. Numerical simulations are compared to experimental data in Figs. 11 and 12.

Although the fits to the two runs used to tune the experimental parameters fit very well, it is clear that, as the strip voltage increased, the fit quality decayed. In Fig. 11, the simulation has been tuned on the uncharged case and the lowest voltage case (run 2: 1000 V on both the strip and the plate). The shape of the strip is still fairly well modeled for runs 3 and 4; however, the strip positions diverge from the actual positions.



**Fig. 12** Results of tuning the model to runs 1 and 4, as well as predicting the positions of runs 2 and 3.



**Fig. 13** Position of experimental strip with  $V_{\text{plate}} = 1 \text{ kV}$  and  $V_{\text{strip}} = 0 \text{ kV}$ . The drift from the original test (yellow) to the left originated after successive charge cycles.

An interesting variation emerges if the system is tuned to the two limiting runs (run 1 and run 4) instead of only the lowest potential runs.

As seen in Fig. 11, the two runs used to tune the experiment are fit very well. However, runs 2 and 3 exhibit a significant underprediction of deflection. This result is consistent with the overprediction seen when tuning to runs 1 and 2 because it indicates the model is overpredicting the influence of electrostatic torques on the strip. Test cases of tuning to runs 2 and 3, 2 and 4, or 3 and 4 exhibited the same trend. Furthermore, higher-charge experiments (up to 2000 V cathode and 6000 V strip potentials) were conducted, but the fits continued to increasingly overpredict deflection as the charge increased.

From Figs. 11 and 12, it is clear that some parameters are being mismodeled, resulting in overprediction of the strip deflection at higher potentials. Although the simulation accounted for all of the forces and torques acting on a pure conductor at equilibrium in an electric field under vacuum, certain physics that occur in dielectrics were not modeled.

When this same behavior was seen in previous atmospheric experiments, it was postulated that large strip voltages were ionizing the air, creating plasma that would then shield the strip from the background electric field [39]. Although this effect cannot be completely ruled out as a factor in previous experiments, all experiments shown in Figs. 11 and 12 were performed in vacuum, precluding this effect.

Two effects, illustrated in Figs. 13 and 14, were observed and investigated as contributors to the modeling errors seen. Both of these figures used strips with no kink introduced. Figure 13 shows that, under seemingly identical charging conditions, the strip experiences different forces and torques. The yellow, rightmost line represents the position of the strip with  $V_{\text{plate}} = 1 \text{ kV}$  and  $V_{\text{strip}} = 0 \text{ kV}$  before the strip was charged. The lines to the left are its position under the same voltage settings after experiments in which the strip was charged to progressively higher voltages. This indicates that the Mylar, which is an insulator (and therefore does not charge and discharge on the fast timescales upon which conductors do), was experiencing polarization due to the high electric fields, and it was accumulating charge as consecutive experiments were performed. This dielectric charging effect is impossible to accurately model for a system such as this because the level of dielectric charge buildup is a product of electric field and strip potential histories, as well as material properties. Therefore, such a model would be even more specific than the one developed here, requiring inputs that are impossible to apply from one run to another.

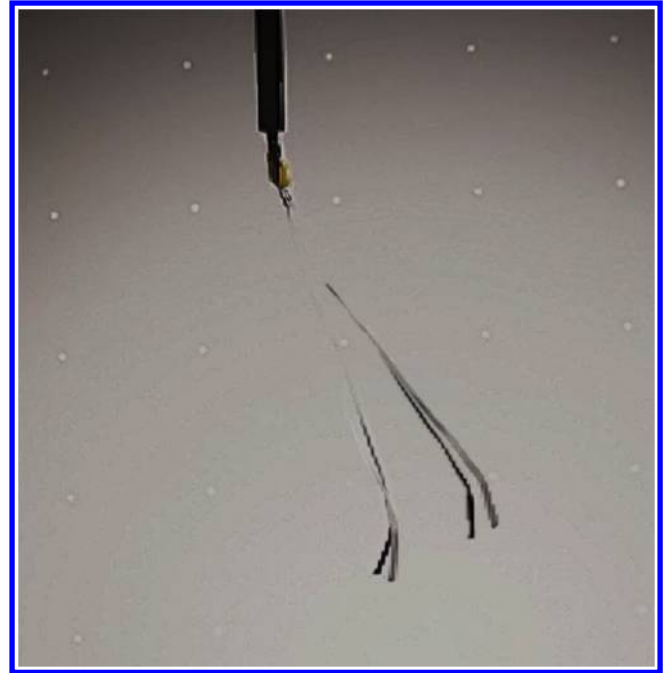


**Fig. 14** Rapid position variations of experimental strip over 0.5 s during a discharge event.

Of more significance to the broader community interested in HAMR objects, Fig. 14 illustrates spontaneous high-amplitude motion of the strip when charged to a high potential. In this case, charging the strip above  $\sim 6400 \text{ V}$  resulted in the behavior seen in the Fig. 14, where the strip would spontaneously and rapidly “kick.” After the kick, the motion would damp out due to internal resistance in the strip, but then a new impulsive kick would occur. These impulses had a period of approximately 33 s. This periodic motion suggests that some charging process with a given time constant was dictating the motion; and when the dielectric of the strip became sufficiently charged, it would undergo an impulsive dynamical excitation and then recharge. Because the charge level where this effect becomes apparent is tied to microscopic-level tears and changes to the edge of the Mylar, it is effectively impossible to model or predict for existing HAMR debris objects. An ammeter capable of microampere resolution connected to the strip power supply showed no significant fluctuation during these kick events, indicating that the strip was discharging stored energy. The low vacuum pressure during these experiments (better than  $10^{-6}$  torr) indicates that atmospheric interactions are unlikely to be the cause. Therefore, a self-discharge event is the expected source of the impulse. These experiments illustrate that, to model charged aluminized Mylar, it is not sufficient to simply account for the electrostatic effects acting on the conductor. The complex physics of dielectric polarization and the discharge to vacuum due to the local charge densities along the frayed edges becoming too high must be included. Knowing such properties for space debris objects such as ripped Mylar sheets is not considered feasible.

Note that this effect dominated the dynamics of the system at just 6.4 kV, which is much lower than prior work has used when estimating the influence of charging on HAMR object orbital dynamics. Hughes and Schaub [28], for instance, used an estimate of  $\sim 30 \text{ kV}$  when considering electrostatic forces and torques on a HAMR object, based on simulations performed by Früh et al. [27]. From these experimental results, it can be inferred that these simulations may be overestimating the level of charging occurring in HAMR objects while neglecting difficult to model but very significant dynamical events that can occur.

## VI. Conclusions

The paper presents a methodology for modeling time-varying conducting structures using an augmented multisphere method. The

time-varying shape is discretized into finite segments, and MSM models are developed for each segment. This approach is suitable for large shape changes, as illustrated through analytical matching of the electric field and capacitance from a one-dimensional line deforming into a ring. This method could be applied to quickly and accurately model the electrostatic forces and torques acting on systems ranging from spacecraft unfolding solar panels to multiple spacecraft flying in close proximity, and up through rendezvous.

To see how well this technique could be applied to challenging mixed dielectric-conductor thin structures, experiments on aluminum Mylar are compared to MSM-based numerical simulations of a pure conductor. All experiments and simulations were conducted using a flat, constant electric field under vacuum. Steady-state deflections of a Mylar strip for various charge levels and a background electric field are computed numerically and determined experimentally. The results indicate that charging of the dielectric Mylar components plays a significant role in the dynamics. Furthermore, electric discharge along rough membrane edges caused considerable dynamical disturbances. Modeling only the charge on the conductor provides a baseline for shape change and deflection, but it is not sufficient to fully predict how such an object would behave in the space environment.

### Acknowledgments

This work was partially supported by U.S. Air Force Office of Scientific Research under grant FA9550-15-1-0407. A previous version of this paper was presented at the AAS/AIAA Astrodynamics Specialist Conference in Snowbird, Utah (19–23 August 2018).

### References

- Cover, J. H., Knauer, W., and Maurer, H. A., "Lightweight Reflecting Structures Using Electrostatic Inflation," U.S. Patent 3,546,706, 1970.
- Stiles, L. A., Schaub, H., Maute, K., and Moorer, D. F., "Electrostatic Inflation of Membrane Space Structures," *AIAA/AAS Astrodynamics Specialist Conference*, AIAA Paper 2010-8134, Aug. 2010.
- Stiles, L. A., Schaub, H., Maute, K. K., and Moorer, D. F., "Electrostatically Inflated Gossamer Space Structure Voltage Requirements Due to Orbital Perturbations," *Acta Astronautica*, Vol. 84, March–April 2013, pp. 109–121.  
<https://doi.org/10.1016/j.actaastro.2012.11.007>
- King, L. B., Parker, G. G., Deshmukh, S., and Chong, J.-H., "Study of Interspacecraft Coulomb Forces and Implications for Formation Flying," *Journal of Propulsion and Power*, Vol. 19, No. 3, May–June 2003, pp. 497–505.  
<https://doi.org/10.2514/2.6133>
- Schaub, H., Parker, G. G., and King, L. B., "Challenges and Prospect of Coulomb Spacecraft Formation Control," *Journal of the Astronautical Sciences*, Vol. 52, Nos. 1–2, Jan.–June 2004, pp. 169–193.
- Wang, S., and Schaub, H., "Coulomb Control of Nonequilibrium Fixed Shape Triangular Three-Vehicle Cluster," *Journal of Guidance, Control, and Dynamics*, Vol. 34, No. 1, Feb. 2011, pp. 259–270.  
<https://doi.org/10.2514/1.47835>
- Wang, S., and Schaub, H., "Electrostatic Spacecraft Collision Avoidance Using Piece-Wise Constant Charges," *Journal of Guidance, Control, and Dynamics*, Vol. 33, No. 2, March–April 2010, pp. 510–520.  
<https://doi.org/10.2514/1.44397>
- Hogan, E., and Schaub, H., "Collinear Invariant Shapes for Three-Craft Coulomb Formations," *Acta Astronautica*, Vol. 72, March–April 2012, pp. 78–89.  
<https://doi.org/10.1016/j.actaastro.2011.10.020>
- Bennett, T., and Schaub, H., "Contactless Electrostatic Detumbling of Axi-Symmetric GEO Objects with Nominal Pushing or Pulling," *Advances in Space Research*, Vol. 62, No. 11, Dec. 2018, pp. 2977–2987.  
<https://doi.org/10.1016/j.asr.2018.07.021>
- Bennett, T., Stevenson, D., Hogan, E., McManus, L., and Schaub, H., "Prospects and Challenges of Touchless Electrostatic Detumbling of Small Bodies," *Advances in Space Research*, Vol. 56, No. 3, Aug. 2015, pp. 557–568.  
<https://doi.org/10.1016/j.asr.2015.03.037>
- Bennett, T., and Schaub, H., "Contactless Electrostatic Detumbling of Axi-Symmetric GEO Objects with Nominal Pushing or Pulling," *Advances in Space Research*, Vol. 62, No. 11, 2018, pp. 2977–2987.  
<https://doi.org/10.1016/j.asr.2018.07.021>
- Bennett, T., and Schaub, H., "Touchless Electrostatic Three-Dimensional Detumbling of Large GEO Debris," *Journal of Astronautical Sciences*, Vol. 62, No. 3, Sept. 2015, pp. 233–253.  
<https://doi.org/10.1007/s40295-015-0075-8>
- Aslanov, V. S., "Chaotic Dynamics of a Satellite with Flexible Appendages in the Coulomb Interaction," *Journal of Guidance, Control, and Dynamics*, Vol. 41, No. 2, 2017, pp. 565–572.
- Aslanov, V. S., "Exact Solutions and Adiabatic Invariants for Equations of Satellite Attitude Motion Under Coulomb Torque," *Nonlinear Dynamics*, Vol. 90, No. 4, Dec. 2017, pp. 2545–2556.  
<https://doi.org/10.1007/s11071-017-3822-5>
- Aslanov, V., and Yuditsev, V. V., "Motion Control of Space Tug During Debris Removal by a Coulomb Force," *Journal of Guidance, Control, and Dynamics*, Vol. 41, No. 7, 2018, pp. 1476–1484.  
<https://doi.org/10.2514/1.G003251>
- Aslanov, V. S., "Spatial Dynamics and Control of a Two-Craft Coulomb Formation," *Journal of Guidance, Control, and Dynamics*, Sept. 2019.  
<https://doi.org/10.2514/1.G004382>
- Aslanov, V., and Schaub, H., "Detumbling Attitude Control Analysis Considering an Electrostatic Pusher Configuration," *Journal of Guidance, Control, and Dynamics*, Vol. 42, No. 4, April 2019, pp. 900–909.  
<https://doi.org/10.2514/1.G003966>
- Stevenson, D., and Schaub, H., "Multi-Sphere Method for Modeling Electrostatic Forces and Torques," *Advances in Space Research*, Vol. 51, No. 1, Jan. 2013, pp. 10–20.  
<https://doi.org/10.1016/j.asr.2012.08.014>
- Stevenson, D., and Schaub, H., "Optimization of Sphere Population for Electrostatic Multi Sphere Model," *IEEE Transactions on Plasma Science*, Vol. 41, No. 12, Dec. 2013, pp. 3526–3535.  
<https://doi.org/10.1109/TPS.2013.2283716>
- Ingram, G., Hughes, J., Bennett, T., Reilly, C., and Schaub, H., "Volume Multi-Sphere-Model Development Using Electric Field Matching," *Journal of Astronautical Sciences*, Vol. 65, No. 4, 2018, pp. 377–399.  
<https://doi.org/10.1007/s40295-018-0136-x>
- Hughes, J., and Schaub, H., "Rapid Modeling of Electrostatic Forces and Torques Considering Dielectrics," *Journal of Spacecraft and Rockets* (to be published).  
<https://doi.org/10.2514/1.A34413>
- Hughes, J., and Schaub, H., "Heterogeneous Surface Multi-Sphere Models Using Method of Moments Foundations," *Journal of Spacecraft and Rockets*, Vol. 56, No. 4, 2019, pp. 1259–1266.  
<https://doi.org/10.2514/1.A34434>
- Fennell, J. F., Koons, H. C., Leung, M., and Mizera, P., "A Review of SCATHA Satellite Results: Charging and Discharging," U.S. Air Force, Space Division Air Force Systems Command Rept. SD-TR-85-27, Los Angeles Air Force Station, CA, Aug. 1985.
- Mullen, E. G., Gussenhoven, M. S., Hardy, D. A., Aggson, T. A., and Ledley, B. G., "SCATHA Survey of High-Voltage Spacecraft Charging in Sunlight," *Journal of Geophysical Research*, Vol. 91, No. A2, 1986, pp. 1474–1490.  
<https://doi.org/10.1029/JA091iA02p01474>
- Paul, S. N., and Frueh, C., "Space Debris Charging and Its Effect on Orbit Evolution," *AIAA/AAS Astrodynamics Specialist Conference*, Long Beach, CA, 2009, pp. 1–31.
- Hughes, J., and Schaub, H., "Rapid Charged Geosynchronous Debris Perturbation Modeling of Electrodynamical Disturbances," *Journal of the Astronautical Sciences*, Vol. 65, No. 2, 2018, pp. 135–156.
- Fruh, C., Ferguson, D., Lin, C., and Jah, M., "The Effect of Passive Electrostatic Charging on Near-Geosynchronous High Area-to-Mass Ratio Objects," IAC Paper 13, A6,2,8, x19622, Beijing, China, Sept. 2013.
- Hughes, J., and Schaub, H., "Space Weather Influence on Electromagnetic Geosynchronous Debris Perturbations Using Statistical Fluxes," *Space Weather*, Vol. 16, No. 4, 2018, pp. 391–405.  
<https://doi.org/10.1002/swe.v16.4>
- Chanunmsin, S., Ceriotti, M., Fruh, C., and Radice, G., "Orbital Dynamics of Lightweight Flexible Debris," *64th International Astronautical Congress*, IAC Paper 13-A6.2.7, Sept. 2013.
- Chow, P., Hughes, J., Bennett, T., and Schaub, H., "Automated Sphere Geometry Optimization for the Volume Multi-Sphere Method," *AAS/AIAA Spaceflight Mechanics Meeting*, AAS Paper 16-472, Springfield, VA, Feb. 2016.
- Bennett, T., and Schaub, H., "Electrostatically Charged Spacecraft Formation Estimation Using Linearized Relative Orbit Elements," *AAS Spaceflight Mechanics Meeting*, AAS Paper 17-483, Springfield, VA, Feb. 2017.

- [32] Engwerda, H., Hughes, J., and Schaub, H., "Remote Sensing for Planar Electrostatic Characterization Using the Multi-Sphere Method," *Final Stardust Conference*, Springer, New York, Oct.–Nov. 2016, pp. 145–161.
- [33] Bengtson, M., and Schaub, H., "Remote Sensing of Spacecraft Potential at Geosynchronous Orbit using Secondary and Photo Electrons," *AIAA Science and Technology Forum and Exposition*, AIAA Paper 2019-0311, Jan. 2019.
- [34] Wilson, K. T. H., and Schaub, H., "X-Ray Spectroscopy for Electrostatic Potential and Material Determination of Space Objects," *IEEE Transactions on Plasma Science*, Vol. 47, No. 8, 2019, pp. 3858–3866. <https://doi.org/10.1109/TPS.2019.2910576>
- [35] Smythe, W. R., *Static and Dynamic Electricity*, 3rd ed., McGraw–Hill, New York, 1968, pp. 27–37.
- [36] Jackson, J. D., "Charge Density on Thin Straight Wire, Revisited," *American Journal of Physics*, Vol. 68, Aug. 2000, Paper 789. <https://doi.org/10.1119/1.1302908>
- [37] Thomas, T., "The Capacitance of an Anchor Ring," *Australian Journal of Physics*, Vol. 7, No. 2, 1954, Paper 347. <https://doi.org/10.1071/PH540347>
- [38] Zypman, F. R., "Off-Axis Electric Field of a Ring of Charge," *American Journal of Physics*, Vol. 74, No. 4, 2006, pp. 295–300. <https://doi.org/10.1119/1.2149869>
- [39] Maxwell, J., and Schaub, H., "Applicability of the Multi-Sphere Method to Flexible One-Dimensional Conducting Structures," *AAS/AIAA Astrodynamics Specialist Conference*, AAS Paper 17-618, Springfield, VA, Aug. 2017.
- [40] Kumar, K., "Review on Dynamics and Control of Nonelectrodynamic Tethered Satellite Systems," *Journal of Spacecraft and Rockets*, Vol. 43, No. 4, 2006, pp. 705–720. <https://doi.org/10.2514/1.5479>
- [41] Lammens, N., Kersemans, M., Luyckx, G., Van Paepegem, W., and Degrieck, J., "Improved Accuracy in the Determination of Flexural Rigidity of Textile Fabrics by the Peirce Cantilever Test (ASTM D1388)," *Textile Research Journal*, Vol. 84, No. 12, 2014, pp. 1307–1314. <https://doi.org/10.1177/0040517514523182>

Y. Xu  
Associate Editor